SciMedCentral

Chemical Engineering & Process Techniques

Research Article

Efficient Removal of Azo Dyes by Eco-Friendly Rare-Earth Cross-Linked Sodium Alginate Polymer Gel Spheres: Equilibrium Isotherms, Kinetics and Regeneration Performance Study

Chen Chen[1,2], Shuo Zhao[1,2], Xiaoyu Fan[1], Shuwei Xia[2], and Liangmin Yu[2-4]*

[1]*School of Chemistry and Chemical Engineering, Jining Normal University, China*

[2]*Key Laboratory of Marine Chemistry Theory and Technology, Ministry of Education, College of Chemistry and Chemical Engineering, Ocean University of China, China*

[3]*Open Studio for Marine Corrosion and Protection, Pilot National Laboratory for Marine Science and Technology (Qingdao), China*

[4]*Key Laboratory of Ocean Observation and Information of Hainan Province, Sanya Oceanographic Institution, China*

***Corresponding author**

Liangmin Yu, Key Laboratory of Marine Chemistry Theory and Technology, Ministry of Education, College of Chemistry and Chemical Engineering, Ocean University of China, China

Submitted: 30 March, 2025

Accepted: 29 June, 2025

Published: 30 June, 2025

ISSN: 2333-6633

Keywords

- Sodium Alginate
- Neodymium Ion
- Azo Dyes
- Adsorption
- Printing and Dyeing Wastewater

Abstract

In order to produce efficient green adsorbent materials, neodymium alginate (SA/Nd) gel spheres were prepared by crosslinking sodium alginate reaction with rare earth ions using the droplet polymerization method. The prepared materials were characterized and analyzed by SEM-EDS, XRD, TGA, FT-IR, UV-Vis, BET-BJH and XPS, and the adsorption performance of SA/Nd on azo dyes in water was investigated. The results show that SA/Nd has a pleated structure with abundant oxygen-containing functional groups. The adsorption of 1200 mg/L of Direct Blue GL (DB 151) and Direct Orange 26 (DO 26) reached 1325 mg/L and 1175 mg/g, respectively, under the optimal conditions. After seven desorption and recycling of the adsorbent material, the removal rate of the two azo dyes remained above 80%. SA/Nd mainly realizes efficient adsorption of dyes through electrostatic, hydrogen bonding and complexation, and the above results can provide a reference for the treatment of printing and dyeing wastewater.

INTRODUCTION

With the rapid development of the textile industry, the types and quantities of dyes are increasing, and the treatment of printing and dyeing wastewater has become a focal point to which society must pay great attention [1,2]. The most widely used class of direct azo dyes in the printing and dyeing process can seriously affect the health of those who come into contact with them, such as inducing allergies, carcinogenicity, teratogenicity and environmental pollution [3]. Therefore, azo dye wastewater must be harmlessly treated before discharge [4]. Printing and dyeing wastewater treatment technology mainly includes physical, chemical and biological technologies [5]. In contrast, the physical technology of the adsorption method is widely used because of its convenient operation, high wastewater treatment efficiency and low energy consumption [6,7]. Traditional adsorbents for the treatment of dyeing wastewater, including activated carbon, zeolite and polymeric materials, are very effective for the treatment of low-concentration dye wastewater [8]. However, there are still some problems in the application of adsorbents, such as the high cost, the inability to adsorb high-concentration target dyes selectively, the difficulty of desorbing and regenerating for recycling, and the difficulty of separating the powdered adsorbent from the aqueous phase after adsorption of the pollutants and the risk of generating secondary contamination [9-11]. Therefore, the research and development of cost-effective green adsorbent materials can selectively adsorb high concentrations, can be regenerated and recycled, and can

be easily separated [12]. Non-polluting is the key to solving the problem of its better application [13].

In recent years, biopolymers have been widely used as adsorbent materials in the field of wastewater treatment due to their advantages of high efficiency, environmental protection, non-toxicity and harmlessness [14,15]. Sodium alginate is a kind of polyanionic polysaccharide sodium salt (polymerization) extracted from natural brown algae kelp or sargassum, with the characteristics of hydrophilicity, gelation, non-toxicity, degradability, etc [16,17]. SA contains a large number of -COOH and -OH; the bivalent and above metal cations can be polymerized with it so that the inter-chain connection is more compact and can form microspheres with a three-dimensional network structure. There are significant gaps in the hydrogel structure, called "egg-box structure"[18]. According to the relevant literature, SA materials have shown excellent performance in the adsorption and removal of different types of organic and inorganic pollutants, such as the removal of heavy metal ions Hg(II), Cu(II), Cr(II), Pb(II), etc [19]., and organic dyes methylene blue, methyl orange, etc. [20-22], from wastewater. Therefore, the ideal composites with better adsorption and separation properties can be prepared using SA as the matrix [23]. The unique electronic structure, ionic radius and physicochemical properties of rare earth element atoms can be combined with organic or inorganic functional groups through coordination bonds to form rare earth composite adsorbents with better stability and adsorption performance [24]; meanwhile, the adsorbents containing rare earth ions have the characteristics of high selectivity, good adsorption effect, easy regeneration, etc. [19-25], and have a wide range of prospects for application in the treatment of printing and dyeing wastewater [26,27]. Therefore, the study of rare earth composite adsorbent has specific practical significance in the treatment of printing and dyeing wastewater [28].

Based on the above analysis, in this study, the polymer gel sphere adsorbent material (SA/Nd) containing rich functional groups was prepared by using sodium alginate as the raw material, utilizing its gel property, and adopting rare earth neodymium ionic solution as the cross-linking agent to react with SA. It was used to simulate the adsorption of the wastewater of dye Direct Blue 151 and Direct Orange 26 directly to assess the adsorption performance of the gel sphere adsorbent material. The preparation and adsorption conditions of the adsorbent material were investigated in detail. The adsorption kinetics, isothermal adsorption, adsorption thermodynamics and adsorption mechanism were investigated, with the expectation of providing a feasible way for the preparation of polymer composite adsorbents under rare earth with simple preparation method, a new type of environmentally friendly and high-efficiency adsorption.

MATERIALS AND METHODS

Materials

Sodium alginate (SA, A.R.) was purchased from China National Pharmaceutical Group Chemical Reagent Co. Neodymium (III) nitrate hexahydrate ($Nd(NO3)3{\cdot}6H2O$, A.R.) was purchased from Aladdin Biochemical Technology Co. Direct Blue 151 (DB 151, Direct dye, $C34H25N5Na2O10S2$, Mr = 773.69 g/mol, λmax = 562 nm) and Direct Orange 26 (DO 26, Direct dye, $C33H22N6Na2O9S2$, Mr = 756.67 g/mol, λmax = 495 nm) were purchased from Shanghai Ltd. The structural formulae of the two direct dyes are shown in Figure 1.

Preparation of Sa/Nd Gel Sphere Adsorbent Material

Through detailed investigation, the optimized preparation scheme of SA/Nd gel spheres adsorbent material was as follows (Figure 2): 2 g of SA powder was added into 100 ml of deionized water and stirred continuously for 30 min at 298 K to obtain 0.2 g/L of SA solution, after static defoaming, the obtained SA solution was dropped uniformly into 100 mL of Nd-ion solution through a syringe at 298 K, and the light yellow gel spheres were found to be generated in the solution with uniform sizes. After curing and cross-linking for 2h, the gel spheres were removed from the solution, washed repeatedly with deionized water until neutral, and filtered and dried to obtain the product SA/Nd gel spheres adsorbent material.

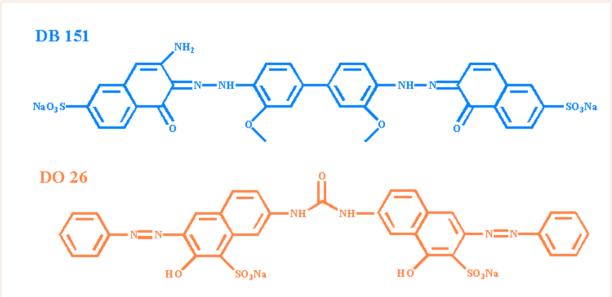

Figure 1 The chemical structures of DB 151 and DO 26

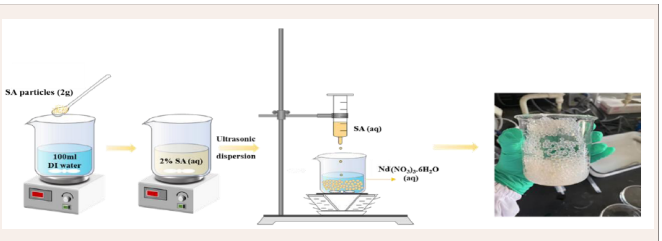

Figure 2 Flow chart of SA/Nd gel spheres preparation

Characterization

Scanning electron microscopy and energy dispersive spectroscopy characterized the surface morphology and elemental distribution of SA and SA/Nd gel sphere adsorbent materials (SEM-EDS, Hitachi SU8010, Japan). X-ray diffraction (XRD) analysis was performed using a Bruker D8 Advance powder diffractometer to examine the physical phase structure of the samples using Cu-Ka radiation with a 2θ range of 5-80°. Fourier transform infrared (FTIR) measurements were performed with a Bruker Tensor II FTIR spectrometer (KBr tableting method, Bruker, Germany), scanning measurements with a resolution of 4 cm-1 over a wave number range of 4000-400 cm^{-1}. The zeta potential was obtained using a Nano-zs Zeta Analyzer (Malvern Panalytical Inc., UK). Specific surface area and pore size of SA/Nd gel spheres were analyzed by Micromeritics ASAP 2460 (Mack Instrument Company, USA) Pore Structure Specific Surface Area Analyzer, Specific surface area was calculated by the Brunauer-Emmett-Teller equation, and the Barrett Joyner Halenda model analyzed pore size. The Thermo Scientific K-Alpha model X-ray photoelectron spectrometer (Thermo Fisher Scientific Inc., USA) was used to characterize the materials and analyze the elemental composition of the sample surface and its chemical state. The thermal stability of SA and SA/Nd materials was examined using a STA499-F3 thermogravimetric analyzer (TGA, netzsch Inc., Germany). Ultraviolet-visible spectroscopy (UV-Vis DRS) analyses were performed by a Shimadzu UV-3600 UV-Vis diffuse reflectance spectrometer (BaSO4 tableting method, Hitachi, Japan).

Adsorption Experiment

To prepare simulated dye wastewater, accurately weigh a certain mass of DB 151 and DO 26 dyes and configure them into 1.4g/L and 1.25g/L reserve liquid, respectively.

0.03g dried SA/Nd gel balls were added into a series of 50 mL conical bottles, and then 25mL direct dye solution with a certain concentration was added respectively. The samples were oscillated in a 298k constant temperature water bath for 120 min, and then filtered with a water filter membrane with a pore size of 0.45μm. The absorbance A of the solution after gel ball removal was measured at the maximum wavelength λmax of each dye by absorbance spectrophotometry, and the equilibrium adsorption capacity Qe(mg/g) and removal rate η(%) of the SA/Nd gel ball adsorption material for the two direct dyes were calculated by formulas (1) and (2), respectively.

$$Q_e = \frac{(C_0 - C_e)V}{m} \quad (1)$$

$$\eta = \frac{(C_0 - C_e)}{C_0} \times 100\% \quad (2)$$

where C0 and Ce respectively represent the initial concentration of dye in solution and the concentration when adsorption reaches equilibrium, mg/L; V represents the volume of the dye solution, L; m represents the mass of SA/Nd adsorption material, g.

In the experiment, the adsorption experiment of each adsorption material was repeated at least three times in parallel to ensure the accuracy of the adsorption experiment. The average value of each group was taken as the final result, and the relative standard deviation (RSD) was controlled below 0.3%.

Regeneration of Adsorbents

In order to evaluate the reuse performance of the adsorption material, experiments were carried out under the set adsorption conditions. In each experiment, SA/ER with a certain mass that has reached adsorption saturation was placed in a series of conical bottles, and 25 mL 0.1mol/L hydrochloric acid solution was added to each for regeneration experiment at a suitable temperature. After being oscillated in a water bath at 298K for 60min, the dye is completely desorbed from the adsorbent, extracted and filtered, and washed with deionized water to neutral, dried in the oven at 80°C, and the regenerated gel ball is obtained. These regenerated gel spheres will be re-tested according to the previously set adsorption experimental procedure, and the adsorption capacity (Qe) will be calculated to determine their recycling capacity.

RESULTS AND DISCUSSION

Characterization Analysis of Adsorbed Materials

The SEM maps of SA and SA/Nd are shown in Figure 3. From the small upper right panel in Figure 3(a), it can be seen that SA is a white powdery solid, and the SEM image of SA is found to be an irregular solid phase, which consists of some lumps, rods, and irregular particles after magnification at 130×; Figure 3(d) shows the wet gel spheres after cross-linking of SA with Nd ions, which are transparent color particles with smooth surfaces, and after oven drying the gel spheres become smaller in size and appear as uniformly sized yellowish spheres (Figure 3(e)), and magnification at 65 × (Figure 3(b)) and 500 × (Figure 3(c)) reveals that the surface of the SA/Nd gel spheres made from SA as a matrix exhibits a large number of grooves of varying depths and fancy folded structures, and this surface morphology is very favorable for the adsorption of pollutants.

To further determine the element composition and distribution of the material, EDS analysis of SA and SA/Nd was performed, and the results are shown in Table 1.

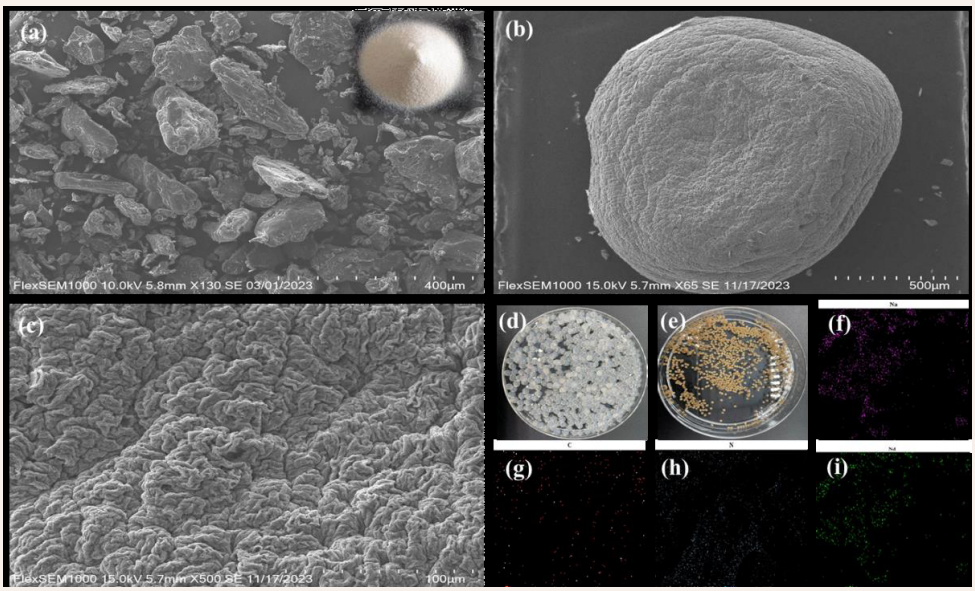

Figure 3 SEM images of SA (a), SA/Nd (b, c); Photograph of wet gel spheres (d) dried gel spheres (e) and distribution of each element of SA/Nd (Na(f), C(g), N(h), Nd(i))

Table 1: EDS analysis of SA, SA/Nd and SA/Nd gel spheres after adsorption of DB 151 and DO 26 dyes

Sample	Element content / (wt%)					
	C	O	Na	N	S	Nd
SA	15.28	52.48	32.23	0.00	0.00	0.00
SA/Nd	27.54	64.23	1.02	4.53	0.00	2.68
After adsorption of DB-151	53.55	27.09	2.62	14.15	1.65	0.95
After adsorption of DO-26	49.17	24.95	2.52	20.50	1.78	1.08

Compared with the composition of SA, N and Nd appeared in SA/Nd, and their contents were 4.53% and 2.68%, respectively. The content of the O element increased by 12.26%. The content of Na decreased by 31.21%, indicating that the SA/Nd gel spheres were successfully prepared by the ion exchange reaction between Nd(III) ion and Na(I) in SA and then by cross-linking polymerization reaction. From the surface scan analysis of SA/Nd gel spheres in Figure 3(f-i), it can be seen that elements C, Na, N and Nd are evenly distributed in the composite material, indicating that a uniform polymer is formed with SA, which is consistent with the results of elemental analysis by EDS.

XRD analyzed the SA and SA/Nd gel spheres, the results are shown in Figure 4(a). Compared with PDF#28-0491, the characteristic diffraction peaks at 2θ values of 14.12°, 21.62° and 38.38° are attributed to SA, which proves the amorphous structure of SA. In the XRD pattern of SA/Nd, the diffraction peaks of SA disappear, indicating that Nd(III) has undergone cross-linking polymerization with SA molecular chains to form new substances, resulting in changes in the crystal phase structure of SA.

FT-IR measurements of SA and SA/Nd gel spheres were performed in the range of 500 cm^{-1} to 4000 cm^{-1}, and the results are shown in Figure 4(b). In the FT-IR spectrum of SA, the absorption peak at 3415 cm^{-1} belongs to the -OH stretching vibration peak, the asymmetric and symmetrical stretching vibration absorption peaks of -COOH and the C-O-C stretching vibration peaks appear at 1612 cm^{-1}, 1417 cm^{-1} and 1029 cm^{-1}, respectively. Compared with the FT-IR spectrum of SA, the stretching vibration peak of -OH in the SA/Nd spectrum moved to 3330cm-1 in the direction of low wave number, because the GG segment of the molecular chain formed a coordination structure with Nd(III) after SA formed gel. The formed network structure will limit the -OH stretching vibration on the macromolecule's six-membered ring, resulting in the shift of its peak position. The asymmetric absorption peak of -COOH moved to the low wave number of 1603 cm^{-1}, and the symmetric absorption peak moved to the high wave number of 1434 cm^{-1}, while the characteristic peak area and intensity changed significantly, which was caused by the ion exchange between Nd(III) and Na(I) ions in the

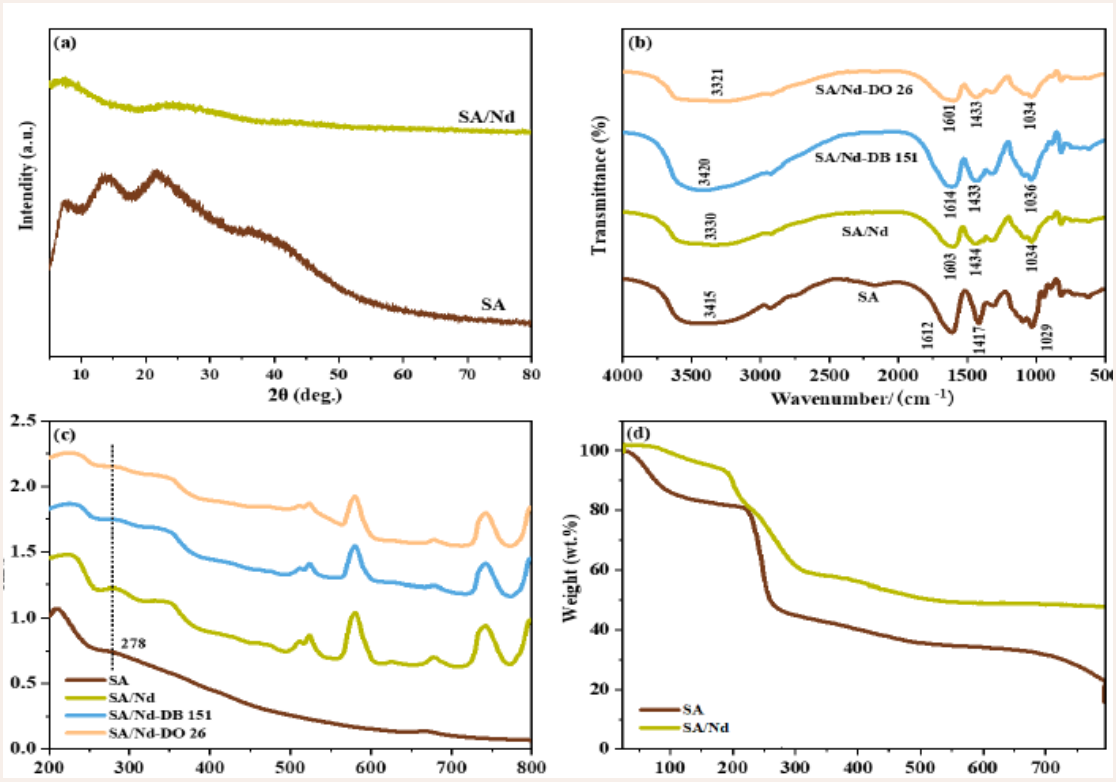

Figure 4 XRD patterns (a) of SA, SA/Nd; FTIR spectra (b) and UV-Vis DRS (c) of SA, SA/Nd and SA/Nd gel spheres after adsorption of DB 151 and DO 26 dyes; TGA profile (d) of SA, SA/Nd

SA molecular chain [29,30]. Furthermore, a polymer with -CO-O-Nd-O-CO-coordination structure was formed by the cross-linking polymerization with -COOH in the SA molecular chain, resulting in a shift in the characteristic peak of -COOH, which further proves that SA/Nd is a network macromolecule formed by the cross-linking of Nd(III). The C-O-C stretching vibration peak moved to the high-wave position of 1034 cm^{-1}, mainly because the interring oxygen on the GG molecular chain in SA also participated in the coordination reaction. The above changes indicate Nd(III) and SA interaction [31].

Figure 4(c) shows the UV-Vis spectra of SA and SA/Nd gel spheres at wavelengths ranging from 200 nm to 800 nm. Compared with the SA spectrum, the absorption spectra of SA/Nd showed new absorption peaks near 520 nm and at 580, 677 and 741 nm, indicating that Nd(III) ions reacted with SA to form a new gel polymer, which was consistent with the analysis results of SEM and FT-IR.

Figure 4(d) shows the TGA curves of SA and SA/Nd. The thermogravimetric analysis curve shows that the total mass of the two materials gradually decreases with the increase in temperature. The pyrolysis of SA/Nd is mainly divided into three stages: (1) in the range of 29-159 °C, part of the free water and surface-bound water of SA/Nd evaporate, and the mass loss is 6%; (2) In the range of 159-339°C, partial dehydration of -OH and -COOH in SA molecules and the breakdown and decomposition of glucoside bonds occurred, and the mass loss at this stage was 36%; (3) In the range of 339-790°C, the further decomposition of intermediate products, the mass loss at this stage is 11%. The decomposition temperature of SA/Nd in the three stages of thermal decomposition is higher than that of SA, and the final mass loss is reduced by 26%. TGA analysis shows that SA/Nd has better thermal stability than SA, which is conducive to storage and use and has potential application value in wastewater treatment.

The chargeability of the surface of the adsorbent material is an important property of the adsorbent material, and the zeta potential versus pH curve for SA/Nd is displayed in Figure 5(a). The isoelectric point (pHIEP)) of SA/Nd is 5.12, at which point the net charge of the adsorbent surface is 0. Combined with the effect of pH on the adsorption performance of SA/Nd (Figure 5(b)), it was analyzed that both direct dyes existed as anions in aqueous solution, and when the pH of the system was less

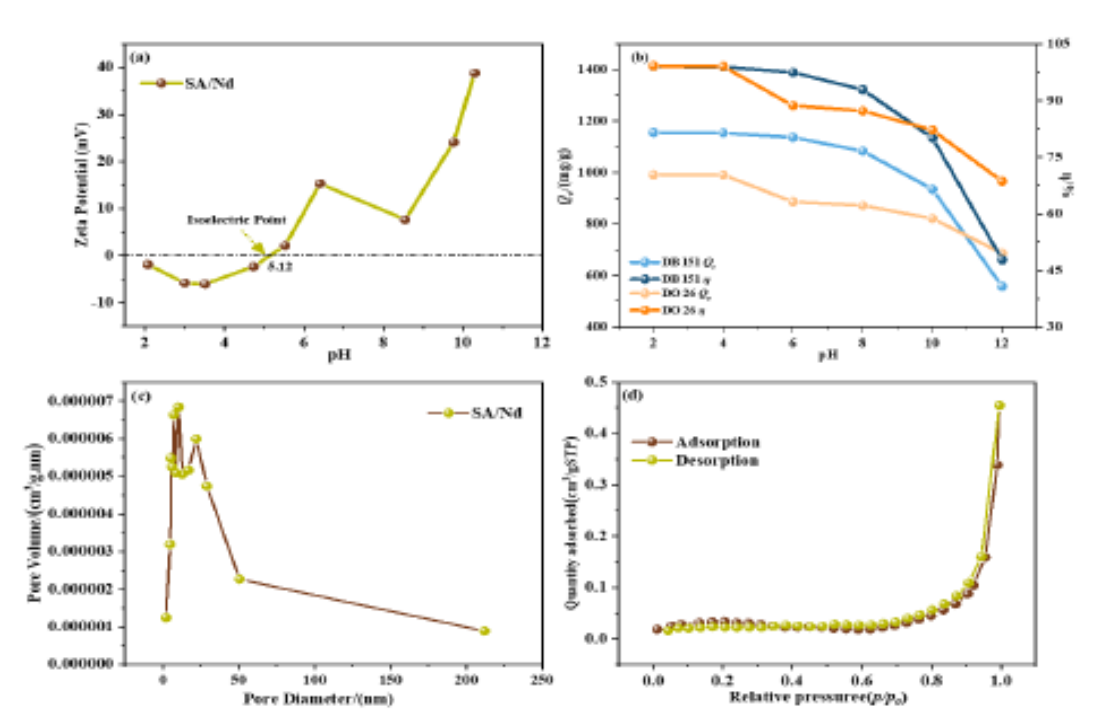

Figure 5 Zeta potential of SA/Nd at different pH values (a); effect of pH on the adsorption performance of SA/Nd (b); pore size distribution (c); adsorption-desorption isotherm (d)

than 5.12, the protonation on the surface of SA/Nd would be enhanced with the decrease of the pH of the solution. The Nd(III) would increase the positive charge density on the surface of the adsorbent, which would significantly increase the electrostatic adsorption capacity between the two. When the pH of the system is more significant than 5.12, with the increase of the pH of the dye solution, there is a competition between -OH in the solution and dye anion adsorption on the surface of SA/Nd, the protonation ability of the gel sphere surface is weakened. The deprotonation ability is enhanced so that the negative electronegativity of the surface of the gel sphere is gradually strengthened with the dye anion, and electrostatic repulsion will be generated, which will decrease the adsorption performance of SA/Nd. However, the -COOH and -OH groups on the surface of SA/Nd can form hydrogen bonds with -N=N- and -OH in the direct dye molecules, so that SA/Nd can maintain a specific adsorption capacity for dye anions under alkaline conditions (pH ≤ 10.0). The zeta potential values of SA/Nd were mainly distributed in the range of -6-39 mV, which indicated that the material remained stable at different pH values.

Specific surface area analysis of SA/Nd using inert N2 adsorption-desorption technique was carried out, and the resulting pore size distribution and isothermal curves are shown in Figure 5 (c-d). According to the figure, it can be seen that the pore size distribution of SA/Nd is mainly concentrated in the range of 2~50 nm. The adsorption-desorption curve of the SA/Nd gel sphere is consistent with the isotherm of type IV in the classification of IUPAC, which is precisely the typical adsorption curve of mesoporous materials, and the curve appears the H3-type hysteresis loop. The results of the two figures indicate that SA/Nd is a kind of adsorbent material with a predominance of mesopores.

Adsorption Kinetics

To investigate the adsorption mechanism of SA/Nd gel spheres on dye molecules, the kinetic experimental data at different temperatures (298 K, 313 K and 328 K) were fitted by using the pseudo-first-order kinetic model and pseudo-second-order kinetic model, and the specific equations of the two models were as follows [32]. The fitting results are detailed in Figure 6(a-b). In contrast, the significant fitting parameters and correlation coefficients (R2) for each kinetic model are listed in Table 2, along with the results of the error analysis (root-mean-square error SD) calculated using Origin software.

$$\ln (Q_e - Q_t) = \ln Q_{e1} - k_1 t \quad (3)$$

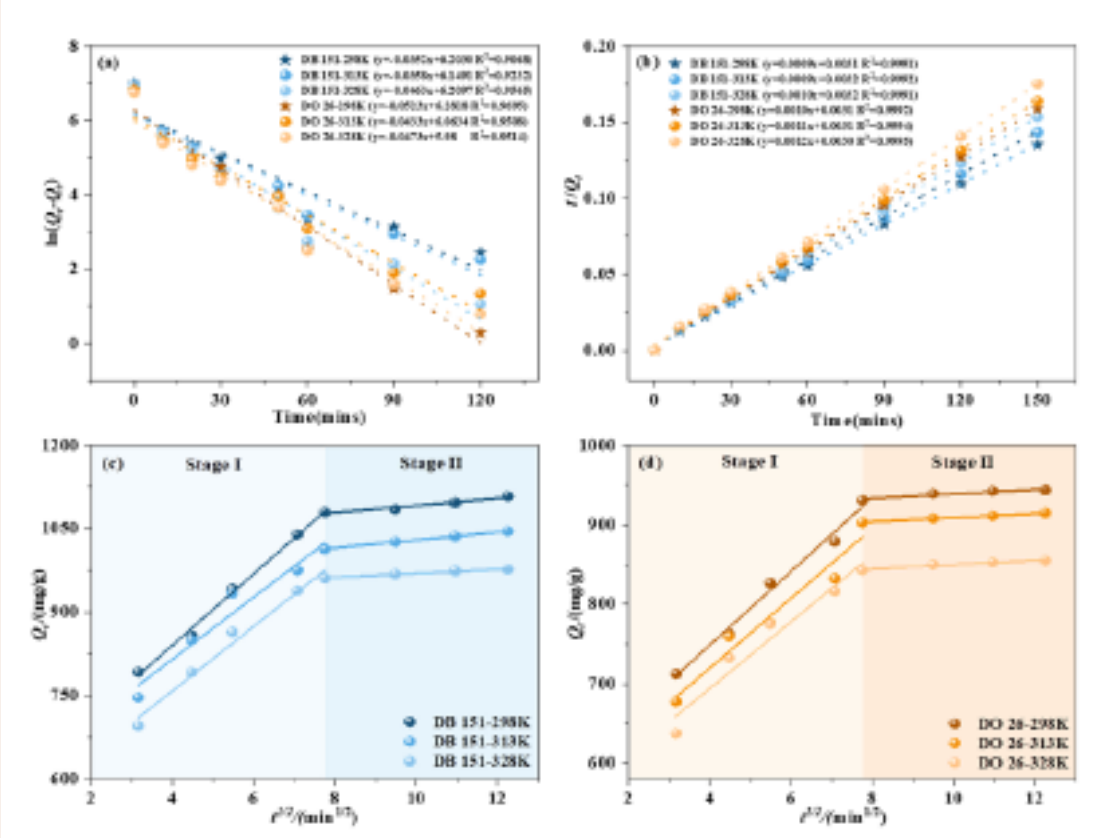

Figure 6 Fitted curves of the proposed primary(a) and secondary kinetics(b) and intra-particle diffusion model(c-d) for the SA/Nd adsorption process

Table 2: Kinetic model fitting parameters of two azo dyes on SA/Nd at different temperatures

Dyes	T (K)		Pseudo-first-order model				Pseudo-second-order model			
		$Q_{e,exp}$ (mg/g)	k_1 (min^{-1})	$Q_{e,1}$ (mg/g)	R^2	SD	k_2 [g/(mg·min)$^{-1}$]	$Q_{e,2}$ (mg/g)	R^2	SD×10^{-4}
DB 151	298	1103	0.0367	331	0.8408	0.50	0.0005	1113	0.9999	7.30
	313	1045	0.0287	158	0.5511	0.46	0.0011	1046	0.9999	5.17
	328	1030	0.0398	94	0.5770	0.44	0.0025	1032	1	2.54
DO 26	298	945	0.0415	269	0.8663	0.41	0.0007	952	0.9999	6.99
	313	921	0.0440	107	0.6086	0.44	0.0019	926	0.9999	4.71
	328	915	0.0384	107	0.6267	0.48	0.0022	917	1	3.02

$$\frac{t}{Q_t} = \frac{1}{k_2 Q_{e,2}^2} + \frac{t}{Q_{e,2}} \quad (4)$$

Where Qe (mg/g) and Qt (mg/g) are the adsorption amounts at adsorption equilibrium and at adsorption time t(min), k1(min-1) and k2[g. (mg.min)$^{-1}$] are the adsorption rate constants for the proposed primary and proposed secondary adsorption models.

Based on the data in Figure 6(a-b) and Table 2, we found that the adsorption kinetic data of SA/Nd adsorbent materials on two azo dyes at different temperatures (298 K, 313 K, 328 K) were by the proposed second-order adsorption rate equations (R2 ≥ 0.9999), and were significantly better than the fitting results of the proposed first-order adsorption rate equations (R2 ≥ 0.5511).

Meanwhile, the equilibrium adsorption amounts (Qe,2) of SA/Nd to the two azo dyes at different temperatures calculated by the proposed second-level adsorption rate equation were very close to the actual measured equilibrium adsorption amounts (Qe,exp). The SDs calculated from the data fitted by this proposed second-level kinetic model were significantly lower than the proposed first-level values. This indicates that the adsorption process of the two dyes on SA/Nd at different temperatures can be accurately described by the proposed

two-stage adsorption kinetic equation, and the fitting results also indicate that the adsorption rates of the two azo dyes on SA/Nd are more susceptible to the influence of chemisorption [33].

The theoretical equilibrium adsorption amount (Qe,c) calculated from the fitting of the second-stage adsorption model and the measured equilibrium adsorption amount (Qe,exp) of SA/Nd on the two azo dyes both showed a decreasing trend with increasing temperature. However, the overall change was small, which indicated that the adsorption operation was suitable for room temperature. In addition, the proposed secondary adsorption rate constant (k2) increased with increasing temperature, which indicated that the adsorption of both azo dyes by SA/Nd was exothermic [34].

Typically, the adsorption process of a material can be divided into two stages, i.e., adsorption on the adsorbent surface and slow diffusion through the pores. In this study, the Weber-Morris intraparticle diffusion model (formulas (5)) was used to fit the adsorption data of two azo dyes on SA/Nd materials to explore the mechanism of the adsorption process in depth. By plotting Qt with t1/2 as the horizontal coordinate, the resulting fitted curves are detailed in Figure 6(c-d), while the corresponding fitting parameters are listed in Table 3.

$$Q_t = k_p t^{\frac{1}{2}} + C \quad (5)$$

Where kp is the internal diffusion constant (in mg/(g.min1/2)), and C denotes a constant related to the thickness of the boundary layer. By plotting a graph with t1/2 as the horizontal coordinate and Qt as the vertical coordinate, the values of kp and C can be determined using the slope and intercept.

As shown in Figure 6(c-d), the adsorption process of SA/Nd on the two azo dyes under different temperature conditions revealed two distinct stages by the fitting curves of the intra-particle diffusion model. This suggests that the adsorption process is divided into multiple steps, with the initial phase mainly consisting of fast or immediate adsorption on the surface of the gel spheres, followed by a slow diffusion phase inside the pores to complete the adsorption gradually. It is noteworthy that these curves do not cross the origin of the coordinates, indicating that intra-particle diffusion is not the only determining step in the adsorption process [35].

Further analysis of the parameter Table 3 revealed that the intra-particle diffusion coefficient kp of SA/Nd decreased from the first to the second stage during the adsorption of the two azo dyes. In contrast, the value of the diffusion boundary layer C increased. This indicates that the dye molecules can diffuse faster to the adsorption sites at the initial adsorption stage due to the thinner diffusion boundary layer and lower diffusion resistance. However, as the adsorption proceeded, the available adsorption sites on the gel spheres were gradually occupied, and the diffusion boundary layer became thicker, which increased the resistance to diffusion and led to the slowing down of the diffusion rate.

Isothermal Adsorption

The isothermal adsorption data for the adsorption of two azo dyes by SA/Nd at different temperatures (298 K, 313 K, 328 K) were fitted by using the Langmuir isothermal model and Freundlich isothermal model, respectively. The model equations are shown in Eqs. (6) and (7), respectively, and the related fitting parameters are shown in Table 4, and the adsorption isotherm of SA/Nd is shown in Figure 7(a).

$$\frac{C_e}{Q_e} = \frac{C_e}{Q_m} + \frac{1}{Q_m K_L} \quad (6)$$

$$ln\, Q_e = \frac{ln\, C_e}{n} + ln\, K_F \quad (7)$$

Where Ce represents the solute concentration in the solution at the adsorption equilibrium (mg/L); Qe is the actual adsorption amount at the adsorption equilibrium (mg/g); Qm is the theoretical maximum adsorption amount at the saturation state (mg/g); and KL stands for the equilibrium constant of the Langmuir adsorption isotherm (L/mg). In the Freundlich model, KF is the

Table 3: Parameters of SA/Nd intra-particle diffusion model fit

Dyes	T (K)	Intraparticle diffusion model					
		k_p (mg/g·min$^{1/2}$)	C	R^2	k_p (mg/g·min$^{1/2}$)	C	R^2
DB 151		0-60 min			60-150 min		
	298	64	584	0.9956	6.44	1028	0.9574
	313	56	592	0.9539	7.03	959	0.9992
	328	58	527	0.9820	3.57	934	0.9853
DO 26		0-60 min			30-150 min		
	298	46	563	0.9875	2.82	911	0.9112
	313	44	544	0.9541	2.59	883	0.9941
	328	42	536	0.9500	2.67	824	0.9496

Table 4: Fitting parameters of isothermal adsorption model for two azo dyes on SA/Nd at different

Dyes	T(K)	temperatures					
		Langmuir model			Freundlich model		
		Q_m(mg/g)	K_L(L/mg)	R^2	1/n	K_F(mg/g)	R^2
DB 151	298	1082	0.0564	0.9989	0.4082	161.33	0.9182
	313	1056	0.0493	0.9991	0.3436	89.82	0.8872
	328	1041	0.0226	0.9992	0.4125	57.92	0.8538
DO 26	298	434	0.0316	0.9984	0.3401	364.28	0.8165
	952	476	0.0248	0.9994	0.3636	133.64	0.7875
	926	416	0.0172	0.9992	0.3676	68.90	0.8452

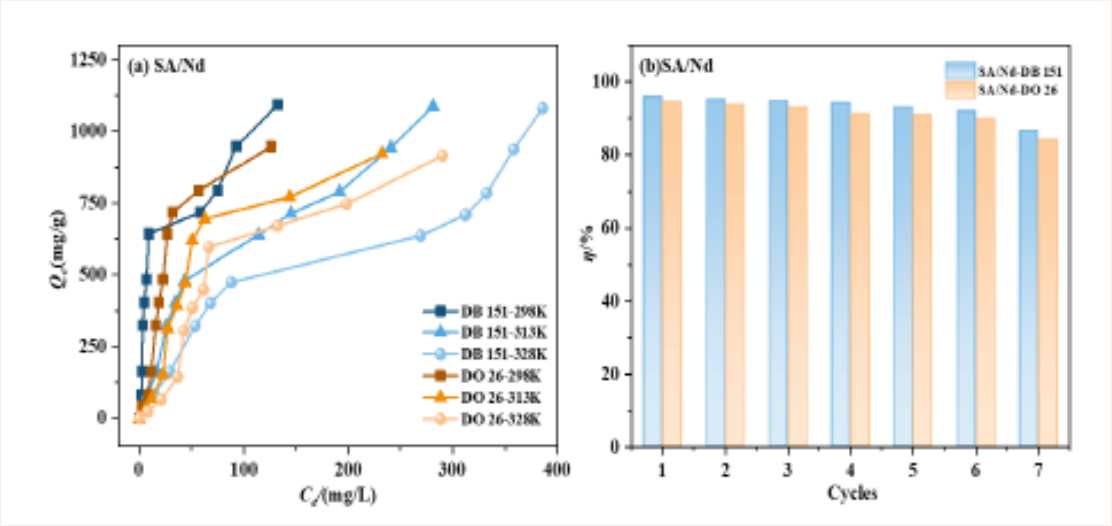

Figure 7 Adsorption isotherms of SA/Nd (a); Effect of the number of cycle regeneration on the adsorption performance (b)

Freundlich adsorption constant in mg/g; n is the index related to the adsorption strength; according to the value of n, the difficulty of adsorption can be judged, n is less than 0.5 means that the adsorption is more difficult, while n between 2 and 10 indicates that the adsorption conditions are more ideal.

As observed in Figure 7(a), the adsorption isotherms of SA/Nd on both azo dyes showed an increasing trend with the increase of the initial concentration of the dyes at a certain temperature. Meanwhile, when the adsorption temperature increased, the adsorption capacity of SA/Nd for both azo dyes showed a decreasing trend, indicating that this adsorption process releases heat, which is consistent with the results of the effect of temperature on adsorption kinetics. According to the fitting data in Table 4, the correlation coefficient R^2 obtained from the Langmuir isothermal model was closer to 1 than that from the Freundlich isothermal model. The maximum adsorption quantities at different temperatures (298 K, 313 K, and 328 K) were more consistent with the saturated adsorption quantities Qm calculated by the Langmuir model, which indicated that the adsorption of SA/Nd on these two azo dyes belongs to monolayer adsorption [36]. In addition, the 1/n value was less than 1, implying that the adsorption conditions were favorable for adsorption. Meanwhile, the adsorption equilibrium constants KL calculated by the Langmuir model and KF obtained by the Freundlich model decreased with the increase in temperature, indicating that the adsorption of the two azo dyes by SA/Nd belongs to the exothermic reaction [37].

Thermodynamics of Adsorption

To further investigate the thermodynamic properties of the SA/Nd adsorption system, the thermodynamic parameters of the two azo dyes on SA/Nd were calculated by applying the Van't Hoff and Gibbs-Helmholtz equations (Eqs. 8-10), and the detailed results are listed in Table 5.

$$\Delta G = -RT\ln K \quad (8)$$

$$\Delta G = \Delta H - T\Delta S \quad (9)$$

$$K = Q_e/C_e \quad (10)$$

Where R represents the gas constant with a value of

Table 5: Thermodynamic parameters of adsorption of SA/Nd on four kinds of azo dyes

Dyes	T(K)	Thermodynamic Parameter		
		ΔG(kJ/mol)	ΔH(kJ/mol)	ΔS(kJ/(mol/K)
DB 151	298	-49.10	-20.59	0.045
	313	-50.35		
	328	-51.66		
DO 26	298	-36.74	-27.47	0.041

8.314 J/mol/K and T is the temperature in Kelvin. The equilibrium constant K can be calculated by applying Eq. 11.

From the data in Table 5, we can learn that at different temperatures, the Gibbs free energy change (ΔG) is less than 0, the enthalpy change (ΔH) is also less than 0, while the entropy change (ΔS) is greater than 0. It is found that the adsorption process of the two dyes on the gel spheres is autonomous and exothermic, and it reduces the ordering of the solid-liquid interface, which suggests that the adsorption is more favorable under the ambient temperature condition. By calculating the thermodynamic parameters of the Van't Hoff equation and Gibbs-Helmholtz equation, we have a more comprehensive understanding of the thermodynamic properties of the adsorption process, which provides strong support for further understanding of the adsorption mechanism. Based on the literature, we understand that the adsorption process mainly involves physical adsorption when the ΔG value is between -20 and 0 kJ/mol, while the adsorption is mainly chemisorption when ΔG is in the range of -80 to -400 kJ/mol. For |ΔH| values in the range of 2-40 kJ/mol, the adsorption is mainly caused by hydrogen bonding; in the range of 2-29 kJ/mol, the adsorption is mainly by dipole moment forces, and in the range of 4-10 kJ/mol, the adsorption is mainly by van der Waals forces [38,39]. The adsorption thermodynamic parameters in Table 5 show that the |ΔH| of SA/Nd on DB 151 and DO 26 dyes are 20.59 and 27.47 kJ/mol, respectively. These data indicate that hydrogen bonding and dipole moment force effects are present between the molecules of SA/Nd on the two azo dyes. The values of ΔG ranged from -51.66 to -27.16 kJ/mol, respectively, suggesting that adsorption material the adsorption of the two azo dyes involves physical, electrostatic adsorption hydrogen bonding and chemisorption.

By comparing the adsorption properties of DB 151 and DO 26 by different adsorption materials (Table 6), it was found that the adsorption properties of SA/Nd were significantly better than those of other adsorption materials, and the preparation process of SA/Nd was simple, the performance was stable, the recycling performance was good, and the adsorption properties were biofriendly.

Cycling-regeneration Performance Study

The regenerative capacity and recyclability of adsorbent materials are important indicators for assessing their practical application potential. As shown in Figure 7(b), the SA/Nd gel spheres could still remove more than 80% of the two azo dyes after seven adsorption-desorption cycling experiments. In addition, before and after the cycling experiments, the structure of the SA/Nd gel spheres remained intact without breaking or disintegration, which indicated that the adsorbent material had good mechanical stability.

Analysis of Adsorption Mechanisms

In order to further investigate the adsorption mechanism of SA/Nd on the two azo dyes, SA/Nd before and after the adsorption of the dyes were analyzed by FT-IR (Figure 4(b)), UV-Vis (Figure 4(c)) and XPS (Figure 8).

Based on the observation in Figure 4(b), it can be seen that after the adsorption of DB 151 and DO 26 by SA/Nd, the prominent characteristic peaks in the FT-IR spectra changed compared with the FT-IR spectra of SA/Nd. Specifically, the telescopic vibrational absorption peak of -OH located at 3330 cm^{-1} was changed in position and intensity to different degrees; the symmetric telescopic vibrational absorption peaks of -COOH at 1603 cm^{-1} were shifted to 1614 and 1601 cm-1, respectively, while the peak absorption intensities increased; The absorption intensity of the antisymmetric telescopic absorption peak of -COOH at 1434 cm^{-1} also increased to different degrees, and the peak shape was slightly broadened; meanwhile, the absorption intensity of the telescopic vibrational absorption peak of -C-O also changed. It was analyzed that the above changes might originate from the multiple hydrogen bonding interactions formed between -COOH and -C-O groups on SA/Nd and -N=N-, -OH, and -COOH in the molecules of the two azo dyes [40].

It can be observed from Figure 4(c), that in the UV-vis spectra of SA/Nd, after adsorption of the materials DB 151 and DO 26 dyes, the characteristic peaks located at around 287, 347 and 341 nm disappear, while the intensity of the characteristic peaks at 523, 581, and 742 nm diminish. This indicates that the dye molecules have bound to the adsorbent and there is a strong interaction.

Table 6: Comparison of adsorption properties of different adsorption materials for DB 151 and DO 26

Dye name	Adsorbents	Maximum adsorption capacity(mg/g)	Reference
DB 151	Camellia sinensis waste	90.9	(Rehman et al. 2017)
	AS-CTAB	394	(Kasperiski et al. 2018)
	zeolite	75	(Khammarnia et al. 2017)
	SA/Nd	1325	This study
DO 26	H_2SO_4- halloysites adsorbent	384.4	(Kusmierek et al. 2020)
	PVA-alginate immobilised	10.03	(Safa et al. 2011)
	anion exchange resin Amberlyst A21	285.6	(Wawrzkiewicz and Kucharczyk 2023)
	Spill-Sorb "Fison" peat	17.7	(Kusmierek et al. 2023)
	SA/Nd	1175	This study

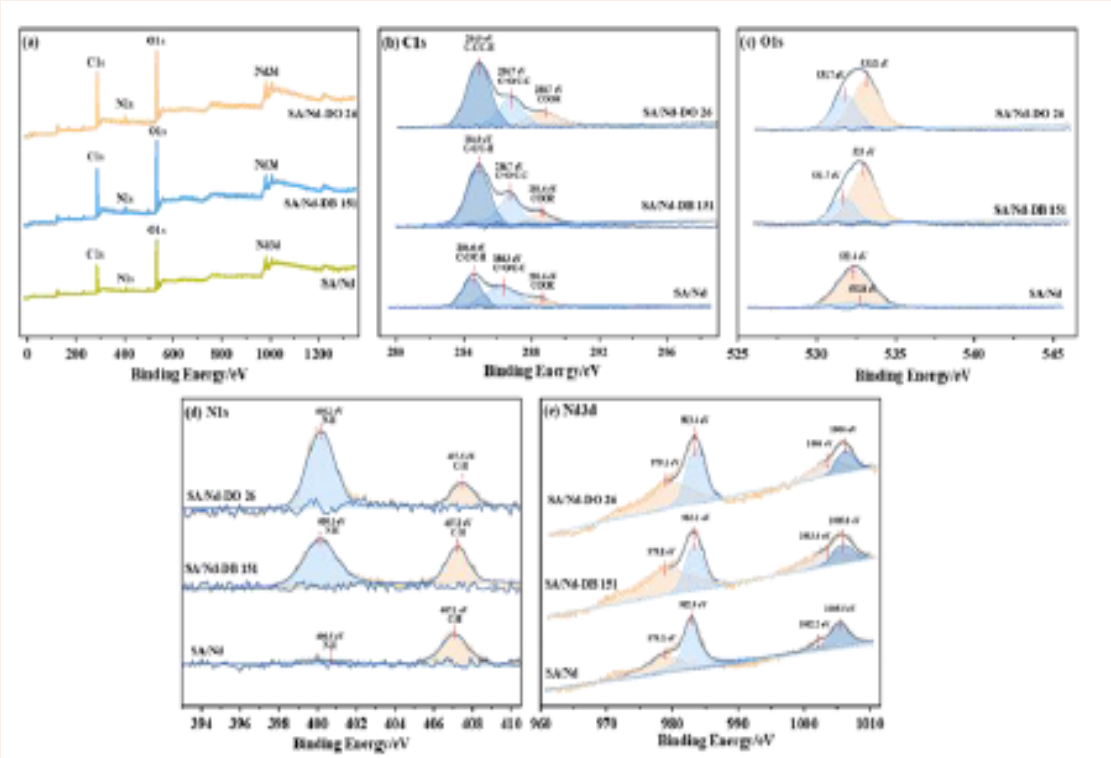

Figure 8 XPS plots of each element before and after dye adsorption on SA/Nd material

By comparing the XPS spectra of the SA/Nd materials before and after adsorption of the DB 151 and DO 26 dyes, the apparent intensity changes of the C, O, N, and Nd peaks indicate the interaction between the adsorbed materials and the dye molecules. Specifically, the XPS spectrum of C1s (Figure 8(b)), shows that the peaks of the C1s orbit can be divided into three categories: C-C, C-H(aromatic), C=O, C-O-C(carbonyl and ether), and -COOH(carboxyl). After dye adsorption, the binding energy of these three peaks increases, and the corresponding core orbital peak area also increases correspondingly, mainly because SA/Nd surface contains -COOH groups, while DB 151 and DO 26 contain azo structure. During the process of SA/Nd adsorbing dyes, the two are prone to interaction. At the same time, the -COOH group also forms strong hydrogen bonding with the -N =N-, -NH-, -NH2 groups in the direct dye molecules, which leads to the increase of binding energy and the expansion of the core orbital peak area. In addition, the XPS spectra of O1s (Figure 8(c)), showed that the binding energy of the O1s peak changed, and the peak area became more extensive after the adsorption of the dyes. This may be because both azo dyes are anionic dyes, and when SA/Nd with a large number of positive charges adsorbs the dyes, strong electrostatic adsorption occurs, which increases the electron density in the outer layer of the gel sphere, enhances the shielding effect, and changes the binding energy of the inner electrons. The XPS spectra of N1s (Figure 8(d)), showed the appearance of N1s core

orbital peaks in the SA/Nd spectra after adsorption of the dye, and the intensity of the C-H peaks was also changed. The XPS spectra of Nd3d (Figure 8(e)), showed an increase in the binding energies of both Nd 3d5/2 and Nd 3d3/2, which suggests that the increase in binding energy may be due to the bonding of -OH bonded to the surface of Nd (i.e., Nd -OH) bonded to the surface of Nd formed hydrogen bonds with the more electronegative atoms such as N, O and S in the direct dye molecule, or Nd-OH underwent an ion-exchange reaction with the dye anion, which is one of the reasons why the adsorption and removal rate of SA/Nd could still maintain high values under alkaline conditions [41-47]. The intense interaction between the SA/Nd gel spheres and the two azo dye molecules can be fully demonstrated by analyzing the changes of binding energies and core orbital peak areas of each element.

Comprehensively analyzing the effect of pH on the adsorption process and the test results of FTIR, UV-Vis and XPS, it can be inferred that the adsorption of SA/Nd to the two azo dye molecules mainly relies on electrostatic adsorption, ion exchange, hydrogen bonding and complexation. These mechanisms of action can promote the adsorption between SA/Nd and anionic dyes to a large extent. As shown in Figure 9, SA/Nd exhibits a very high removal efficiency of anionic dyes thanks to the interplay of these physical and chemical adsorption mechanisms.

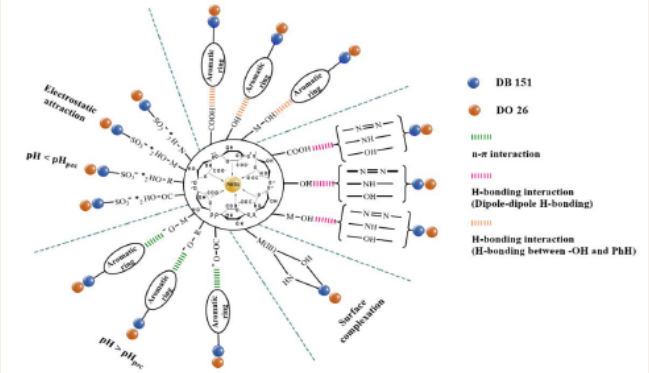

Figure 9 Schematic representation of possible interactions between SA/Nd and dye molecules

CONCLUSION

The SA/Nd synthesized by droplet polymerization can be applied to the efficient purification of azo dye wastewater with large adsorption capacity, fast adsorption rate, short equilibrium time, and suitable for a wide pH range. The adsorption process conformed to the proposed second-order kinetic model, with intra-particle diffusion as the main control step, and the isothermal adsorption satisfied the Langmuir model, and the adsorption process was a spontaneous and exothermic reaction. hydrogen bonding, electrostatic adsorption, and surface complexation were the main interactions between the SA/Nd and the dye molecules, which resulted in a significant adsorption effect on the two azo dyes.

Data availability: Data will be made available on request.

ACKNOWLEDGMENTS

This work was supported by National Natural Science Foundation of China (U22A20112), Hainan Provincial Natural Science Foundation of China (522CXTD520), and the Key Research and Development Project of Hainan Province (ZDYF2021GXJS029).

REFERENCES

1. Zhang H, Li JQ, Cao SC, Ding Y, Wang HT, Chang N. Preparation of Crosslinking-Grafting Cationic Starch Flocculant and Its Study on Textile Dyes Removal. J Polymers Env. 2024; 32: 3407-3421..
2. Beigang L, Chen C. Novel magnetic gel composite based on sodium alginate crosslinked by Yttrium(III) as biosorbent for efficient removal of direct dyes from aqueous solution. J Dispersion Sci Technol. 2021; 43: 1-14.
3. Salem A, Bahadi QA, Drmosh, Sagheer A. Onaizi. Adsorption of anionic and cationic azo dyes from wastewater using novel and effective multicomponent adsorbent. Separation and Purification Technology. 2024; 337: 126402.
4. Zhao Y, Li B. Preparation and Superstrong Adsorption of a Novel La(?)-Crosslinked Alginate/Modified Diatomite Macroparticle Composite for Anionic Dyes Removal from Aqueous Solutions. Gels. 2022; 8: 810.
5. Xuemei Wang, Aitang Zhang, Minghui Chen, Moaaz K. Seliem, Mohamed Mobarak, Zhiquan Diao. Adsorption of azo dyes and Naproxen by few-layer MXene immobilized with dialdehyde starch nanoparticles: Adsorption properties and statistical physics modeling. Chem Eng J. 2023; 473: 145385.
6. Baig N, Shetty S, Bargakshatriya R, Pramanik SK, Alameddine B. Efficient Removal of Carcinogenic Azo Dyes from Water Using Iron(II) Clathrochelate Derived Metalorganic Copolymers Made from a Copper-Catalyzed [4 + 2] Cyclobenzannulation Reaction. Polymers (Basel). 2023; 15: 2948.
7. Sarvalkar PD, Vadanagekar AS, Karvekar OS, Kumbhar PD, Terdale SS, Thounaojam AS, et al. Thermodynamics of Azo Dye Adsorption on a Newly Synthesized Titania-Doped Silica Aerogel by Cogelation: A Comparative Investigation with Silica Aerogels and Activated Charcoal. ACS Omega. 2023; 8: 13285-13299.
8. Liu Z, Khan TA, Islam MA, Tabrez U. A review on the treatment of dyes in printing and dyeing wastewater by plant biomass carbon. Bioresour Technol. 2022; 354: 127168.
9. Chen C, He E, Jia W, Xia S, Yu L. Preparation of magnetic sodium alginate/sodium carboxymethylcellulose interpenetrating network gel spheres and use in superefficient adsorption of direct dyes in water. Int J Biol Macromol. 2023; 253: 126985.

10. Wu J, Liu J, Wen B, Li Y, Zhou B, Wang Z, et al. Nitrogen-rich covalent triazine frameworks for high-efficient removal of anion dyes and the synergistic adsorption of cationic dyes. Chemosphere. 2021; 272: 129622.

11. Muhammad Imran Din, Rida Khalid, Jawayria Najeeb, Zaib Hussain. Fundamentals and photocatalysis of methylene blue dye using various nanocatalytic assemblies- a critical review. J Cleaner Production. 2021; 298: 126567.

12. Metivier-Pignon H, Faur C, Le Cloirec P. Adsorption of dyes onto activated carbon cloth: using QSPRs as tools to approach adsorption mechanisms. Chemosphere. 2007; 66: 887-893.

13. School of Mechanical Engineering, N. Technology, China, and N. U. o. S. T. School of Chemical Engineering, Nanjing 210094, China. Sulfonate-grafted conjugated microporous polymers for fast removal of cationic dyes from water. Chem Eng J. 2020; 391: 123591-123591.

14. Subhadeep Biswas, Anjali Pal. Application of biopolymers as a new age sustainable material for surfactant adsorption: A brief review. Carbohydrate Polymer Technologies and Applications. 2021; 2: 100145.

15. Xinyi Zhu, Liping Bao, Yong Wei, Jiangquan Ma, Yong Kong. Removal of toxic indigo blue with integrated biomaterials of sodium carboxymethyl cellulose and chitosan. Int J Biological Macromolecules. 2016; 91: 409-415.

16. Denis L. Guerra, Rúbia R. Viana, Luiz P. da Costa, Claudio Airoldi. Retraction notice to "Sodium alginate films modified by raw and functionalized attapulgite for use of thorium(IV) adsorption: A thermodynamic approach". J Physics Chem Solids. 2012; 73: 142-142.

17. Abdel-Halim ES, Salem S. Al-Deyab. Removal of heavy metals from their aqueous solutions through adsorption onto natural polymers. Carbohydrate Polymers. 2011; 84: 454-458.

18. Soury R, Jabli M, Latif S, Alenezi KM, El Oudi M, Abdulaziz F, et al. Synthesis and characterization of a new meso-tetrakis (2,4,6-trimethylphenyl) porphyrinto) zinc(II) supported sodium alginate gel beads for improved adsorption of methylene blue dye. Int J Biol Macromol. 2022; 202: 161-176.

19. Qian LW, Yang SF. Zhang C. Hou, Song WQ, Yang JF, et al. Preparation of a sustainable bioadsorbent by modifying filter paper with sodium alginate with enhanced mechanical properties and good adsorption of methylene blue from wastewaters. Cellulose. 2018; 25: 2021-2036.

20. Cho E, Kim J, Park CW, Lee KW, Lee TS. Chemically bound Prussian blue in sodium alginate hydrogel for enhanced removal of Cs ions. J Hazard Mater. 2018; 360: 243-249.

21. Fei-Fei Wang, Hui Yu, Ying-Ying Liu, Guo-Hai Xu, Jian-Fang Ma. Efficient adsorption of organic dyes by two porous heterometallic metal–organic frameworks assembled with Schiff base ligands and Fe 3+ /Cd 2+ ions. Polyhedron. 2018; 156: 188-194.

22. Purbasari A, Ariyanti D, Fitriani E. Adsorption of Methyl Orange Dye by Modified Fly Ash-Based Geopolymer – Characterization, Performance, Kinetics and Isotherm Studies. J Ecological Eng. 2023; 24: 90-98.

23. Zhangsong Jiang, Xiangfeng Huang, Qiaofeng Wu, Mi Li, Qili Xie, Zuwen Liu. Adsorption of sulfonamides on polyamide microplastics in an aqueous solution: behavior, structural effects, and its mechanism. Chem Eng J. 2023; 454: 140452.

24. Mohammadi A, Daemi H, Barikani M. Fast removal of malachite green dye using novel superparamagnetic sodium alginate-coated Fe3O4 nanoparticles. Int J Biol Macromol. 2014; 69: 447-455.

25. Wang Q, Ju J, Tan Y, Hao L, Ma Y, Wu Y, et al. Controlled synthesis of sodium alginate electrospun nanofiber membranes for multi-occasion adsorption and separation of methylene blue. Carbohydr Polym. 2019; 205: 125-134.

26. Xue Sun, Jian Hua Chen, Zhenbo Su, Yihong Huang, Xinfei Dong. Highly effective removal of Cu(II) by a novel 3-aminopropyltriethoxysilane functionalized polyethyleneimine/sodium alginate porous membrane adsorbent. Chem Eng J. 2016; 290:1-11.

27. Rongrui You, Congming Xiao, Li Zhang, Yanrui Dong. Versatile particles from water-soluble chitosan and sodium alginate for loading toxic or bioactive substance. Int J Biol Macromolecules. 2015; 79: 498-503.

28. Zhang H, Wang HT, Yaoyao Z, Li F, Hussain Z, Chang N. Preparation of straw-reinforced grafted starch composite adsorbent for the treatment of textile printing and dyeing wastewater. Textile Res J. 2022; 93: 2002-2017.

29. Qiushi Jiang, Zhaolian Han, Xiaobin Yu, Yafeng Yuan, Yating Ren, Jiapeng Li. NH2-MIL-125 (Ti)/biochar fibers for enhanced direct dyes adsorption. J Env Chem Eng. 2021; 9: 106636.

30. Luan X, Song Z, Xu W, Li Y, Ding C, Chen H. Spectral characteristics on increasing hydrophilicity of Alfalfa seeds treated with alternating current corona discharge field. Spectrochim Acta A Mol Biomol Spectrosc. 2020; 236: 118350

31. Wang B, Lin J, Hu Q, Huang F, Huang Y, Tu W, et al. Adsorption of oxytetracycline on subalpine meadow soil from Zoige Plateau, China: Effects of the coexisting Cu2. Environ Res. 2023; 231: 116221

32. Ahmad AA, Hameed BH, Aziz N. Adsorption of direct dye on palm ash: kinetic and equilibrium modeling. J Hazard Mater. 2007; 141: 70-76.

33. Ruihua Huang, Lujie Zhang, Pan Hu, Jing Wang. Adsorptive removal of Congo red from aqueous solutions using crosslinked chitosan and crosslinked chitosan immobilized bentonite. Int J Biol Macromolecules. 2016; 86: 496-504.

34. Ukkund S, Puthiyillam JP, Anqi AE, Taqui SN, Ali MA, Syed UT, et al. A Recent Study on Remediation of Direct Blue 15 Dye Using Halloysite Nanotubes. Appl Sci. 2021; 11: 23.

35. Álvarez-Gutiérrez N, Gil MV, Rubiera F, Pevida C. Kinetics of CO2 adsorption on cherry stone-based carbons in CO2/CH4 separations. Chem Eng J. 2017; 307: 249-257.

36. Kuśmierek K, Dąbek L, Świątkowski A. Removal of Direct Orange 26 azo dye from water using natural carbonaceous materials. Arch Environmental Protection. 2023; 49: 47-56.

37. Konicki W, Hełminiak A, Arabczyk W, Mijowska E. Removal of anionic dyes using magnetic Fe@graphite core-shell nanocomposite as an adsorbent from aqueous solutions. J Colloid Interface Sci. 2017; 497: 155-164.

38. Sapna Raghav, Dinesh Kumar. Comparative kinetics and thermodynamic studies of fluoride adsorption by two novel synthesized biopolymer composites. Carbohydrate Polymers. 2019; 203: 430-440.

39. Semeraro P, Gabaldón JA, Fini P, Núñez, E, Pellicer JA, Rizzi V, et al. Removal of an Azo Textile Dye from Wastewater by Cyclodextrin-Epichlorohydrin Polymers. In Cyclodextrin - A Versatile Ingredient. 2017.

40. Lv SQ, Liu LJ, Ruan X, Dong J, Zhang LX, Yan G. The Importance of Calcium on the Adsorption of Direct Orange S by Powdered Activated Carbon. Protection of Metals and Physical Chemistry of Surfaces. 2023; 59: 893-898.

41. María Claudia Calderón-Martínez, María Inés Gil-Tolano, Sofía Navarro-Espinoza, Rodrigo Meléndrez, Valery Chernov, Marcelino Barboza-Flores. Optical properties and functional groups

characterization of commercial HPHT micro-diamond samples. Optical Mat. 2022; 131: 112592.

42. Kasperiski FM, Lima EC, dos Reis GS, da Costa JB, Dotto GL, Dias GL, et al. Preparation of CTAB-functionalized aqai stalk and its efficient application as adsorbent for the removal of Direct Blue 15 and Direct Red 23 dyes from aqueous media. Chem Eng Commun. 2018; 205: 1520-1536.

43. Khammarnia SS, Shojaei MG. Pakdel. Study of performance amount of zeolite in the removal of Direct Blue 151 dye from aqueous solutions. Stem Cell. 8.

44. Kusmierek K, Swiatkowski A, Wierzbicka E, Legocka I. Enhanced adsorption of Direct Orange 26 dye in aqueous solutions by modified halloysite. Physicochemical Problems of Mineral Processing. 2020: 56: 693-701.

45. Rehman R, Mahmud T, Ejaz R, Rauf A, Mitu L. Sorptive removal of Direct Blue-15 dye from water using Camellia sinensis and Carica papaya leaves. Bulgarian Chem Commun. 2017; 49: 20-25.

46. Safa Y, Bhatti HN, Bhatti IA, Asgher M. Removal of direct red-31and direct orange-26 by low cost rice husk: influence of immbilisation and pretreatments. Can J Chem Engin. 2011; 89: 1554-1565.

47. Wawrzkiewicz M, Kucharczyk A. Adsorptive Removal of Direct Azo Dyes from Textile Wastewaters Using Weakly Basic Anion Exchange Resin. Int J Mol Sci. 2023; 24: 17.